Single-Cell Protein Interactomes by the Proximity Network Assay

Filip Karlsson[1,*], Michele Simonetti[1], Christina Galonska[1], Max Karlsson[1], Hanna van Ooijen[1], Tomasz Kallas[1], Divya Thiagarajan[1], Maud Schweitzer[1], Ludvig Larsson[1], Vincent van Hoef[1], Pouria Tajvar[1], Johan Dahlberg[1], Florian De Temmerman[2], Louise Leijonancker[1], Sylvain Geny[1], Rikard Forlin[3], Erika Negrini[3], Stefan Petkov[1], Lovisa Franzén[1], Jessica Bunz[1], Christine Moge[1], Henrik Everberg[1], Petter Brodin[3,4,5] , Alvaro Martinez Barrio[1], and Simon Fredriksson[1*]

[1] Pixelgen Technologies AB, Stockholm, Sweden
[2] BioLizard nv, Ghent, Belgium
[3] Department of Women's and Children's Health, Karolinska Institutet, 17165, Solna, Sweden
[4] Department of Immunology and Inflammation, Imperial College London, London, UK
[5] Medical Research Council London Institute of Medical Sciences (LMS), Imperial College Hammersmith Campus, London, UK

*) corresponding authors filip.karlsson@pixelgen.com and simon.fredriksson@pixelgen.com

Abstract

Cellular function depends on dynamic interactions and nanoscale spatial organisation of proteins. While transcriptomic and proteomic methods have enabled single-cell profiling, scalable technologies allowing high-resolution analysis of protein interactions at omics-scale are lacking. Here we present the Proximity Network Assay (PNA), a DNA-based method for constructing three-dimensional nanoscale maps of 155 proteins in single cells without the use of optics. PNA employs barcoded antibodies and *in situ* rolling circle amplification to generate >40,000 spatial nodes per cell, which are linked through proximity-dependent gap-fill ligation and decoded by DNA sequencing, forming single cell Proximity Networks. At an estimated spatial resolution of ~50 nm, PNA captures single-cell protein abundance, self-clustering, and colocalization, validating established cell membrane protein interactions. We illustrate how PNA can be used to gain insights into the molecular mechanisms of cell function through protein interactions in hematological oncology, CAR-T cell therapies, and autoimmune disease.

Introduction

Proteins function in dynamic clusters with other proteins to carry out a wide array of cellular activities, including migration, adhesion, and signal transduction [1–4]. These assemblies encode regulatory states and dynamic interactions that cannot be inferred from molecular abundance alone. Capturing the spatial interactome at high resolution and single-cell resolution remains a fundamental challenge in cell biology and translational research. Approximately 60% of all known drug targets reside in the plasma membrane and are functionally dependent on the nanoscale organisation and clustering of membrane-associated proteins [5,6].

Despite the availability of high-throughput omics technologies for transcript and protein quantification at the single-cell level, scalable tools to measure spatial protein interactions with nanoscale resolution and single-cell granularity are lacking. Imaging-based methods such as fluorescence microscopy and imaging mass cytometry are limited by optical resolution and multiplexing constraints by their reliance on light. Proximity-based methods like *in situ* Proximity Ligation Assay (PLA) and Förster Resonance Energy Transfer (FRET) achieve spatial resolution down to 10–40 nm but are inherently limited to pairwise interactions and low multiplexing [7]. In contrast, mass spectrometry-based approaches such as co-immunoprecipitation (co-IP) or proximity labeling techniques like BioID (proximity-dependent biotin identification) and APEX (engineered ascorbate peroxidase) provide broader, unbiased discovery capabilities [8], but require large, homogeneous cell populations (typically millions of cells), lack spatial resolution, and are incompatible with profiling of heterogeneous clinical samples. Collectively, these limitations have left a critical gap in our ability to study protein interactomics at the scale, resolution, and throughput needed for single-cell and translational research applications.

To address this, we previously introduced Molecular Pixelation (MPX); a DNA-based, optics-free spatial proteomics method that segments the cell surface of individual cells into local interaction zones using barcoded antibody-oligonucleotide conjugates and spatially anchored concatemeric UMIs at ~280 nm resolution [9]. MPX, part of the emerging field of DNA microscopy [9-15], alleviated the limitations of fluorescence multiplexing by encoding spatial proximity in DNA sequence space.

Here, we present the Proximity Network Assay (PNA), a next-generation sequencing-based platform for reconstructing three-dimensional spatial interaction networks of proteins in single cells. PNA builds on the core principle of proximity-based assays such as PLA and PEA [16-18], but moves beyond pairwise designs by introducing multiple spatial contact points per protein target. Each barcode, attached to an antibody, undergoes *in situ* rolling circle amplification (RCA), generating many identical barcode copies that serve as spatial nodes. These nodes are linked to neighboring RCA products via hybridisation of a linker oligonucleotide, followed by gap-fill ligation to generate united barcode pairs. These DNA constructs, representing spatial proximity events, are read out by next-generation sequencing and computationally reconstructed into Proximity Networks; graph-based representations of single-cell spatial proteomes, or Proxiomes.

We demonstrate the performance of PNA by profiling 155 antibody-targeted proteins with the Pixelgen Proxiome kit, generating ~40,000 spatial nodes per cell at an estimated resolution of ~50 nm. PNA avoids the limitations of microscopy readout and integrates with standard NGS workflows. The resulting data structure supports analysis of protein abundance, spatial clustering metrics, and colocalization, allowing for a systems-level view of protein organisation.

We apply PNA to a diverse set of biological systems including peripheral blood mononuclear cells (PBMCs), hematologic cancer cell lines, CAR-T cell models, and autoimmune disease samples, demonstrating its ability to resolve protein interactions, spatial rearrangements, and cell type specific network topologies. By enabling spatial interactome mapping of thousands of single cells in clinical and experimental samples, PNA opens a new dimension for studying protein networks at scale, with direct applications in systems immunology, drug target discovery, biomarker discovery, and translational research.

Results

Proximity Network Assay

PNA operates in suspension, using standard molecular biology workflows (**Figure 1A**). PFA fixed cells are bound by barcoded antibodies (Ab-BC) targeting surface proteins. Each Ab-BC exists in two versions (type-1 and type-2) with distinct oligonucleotide sequences to avoid downstream self-interaction events. These oligonucleotides carry a Protein ID (PID) and a unique molecular identifier (UMI), and are hybridized by type-1 or type-2 gap-fill ligation padlock probes to which the PID and UMIs are copied upon circularization. The circularized padlock is amplified by a short *in situ* rolling circle amplification (RCA), generating a localized cluster of repeated barcode copies anchored at the site of protein binding (**Figure 1A**).

To detect spatial proximity events, linker oligonucleotides are introduced that hybridize to two RCA products in proximity to each other; one type-1 and one type-2. A gap-fill ligation step then incorporates both barcodes (PID + UMI) from each RCA product onto the hybridized linker oligonucleotide along with primer sites for PCR to enable sequencing (**Figure 1B**). Thus, each generated DNA fragment represents a proximity link between two proteins.

Unlike methods that require physical isolation of single cells (e.g. droplet barcoding or imaging), PNA does not require compartmentalization. Instead, each cell is represented by a unique combination of tens of thousands of interconnected UMIs making up its Proximity Network. As a result, thousands of cells can be assayed together in one tube, and later deconvoluted into single-cell Proximity Networks representing the spatial arrangement of the 155 targeted proteins.

The resulting product is a densely connected network for each single cell (**Figure 1C**). To demonstrate the cohesion of the network, the PNA protocol was conducted using fluorescently labeled nucleotides during the *in situ* RCA reactions, and visualized by microscopy **(Supplementary Figure 1**). The PNA reaction products localized specifically to the cell membrane of each single cell and demonstrated even coverage over the entire cell surface.

Since the generated Proximity Networks are spatially resolved, PNA enables not only analysis of protein abundance, but also analysis of spatial patterns across cells, such as spatial self-clustering of each protein and colocalization between different proteins. Due to the intrinsically high multiplex, the assay uniquely profiles the spatial relationships of thousands of protein pair combinations on single cells, simultaneously. The spatial resolution of the method is estimated to 50 nm by dividing the surface area of a lymphocyte, 92 um^2, by the approximately 40,000 unique spatial positions of each cell network [19].

We developed a Proximity Score based on the join count statistic [20] to summarize the level of self clustering or colocalization of proteins. Comparison of the observed join counts with a null distribution from random permutations uniquely adjusts for abundance-driven colocalization and allows for statistical interpretation of significance of each observation. This ability to study colocalization and clustering in isolation from abundance is challenging in many commonly used methods for protein interaction analyses such as *in situ* PLA, fluorescence-based colocalization, proximity labeling, or FRET. Abundance level data in PNA can be analyzed in a similar fashion as other single-cell abundance based methods.

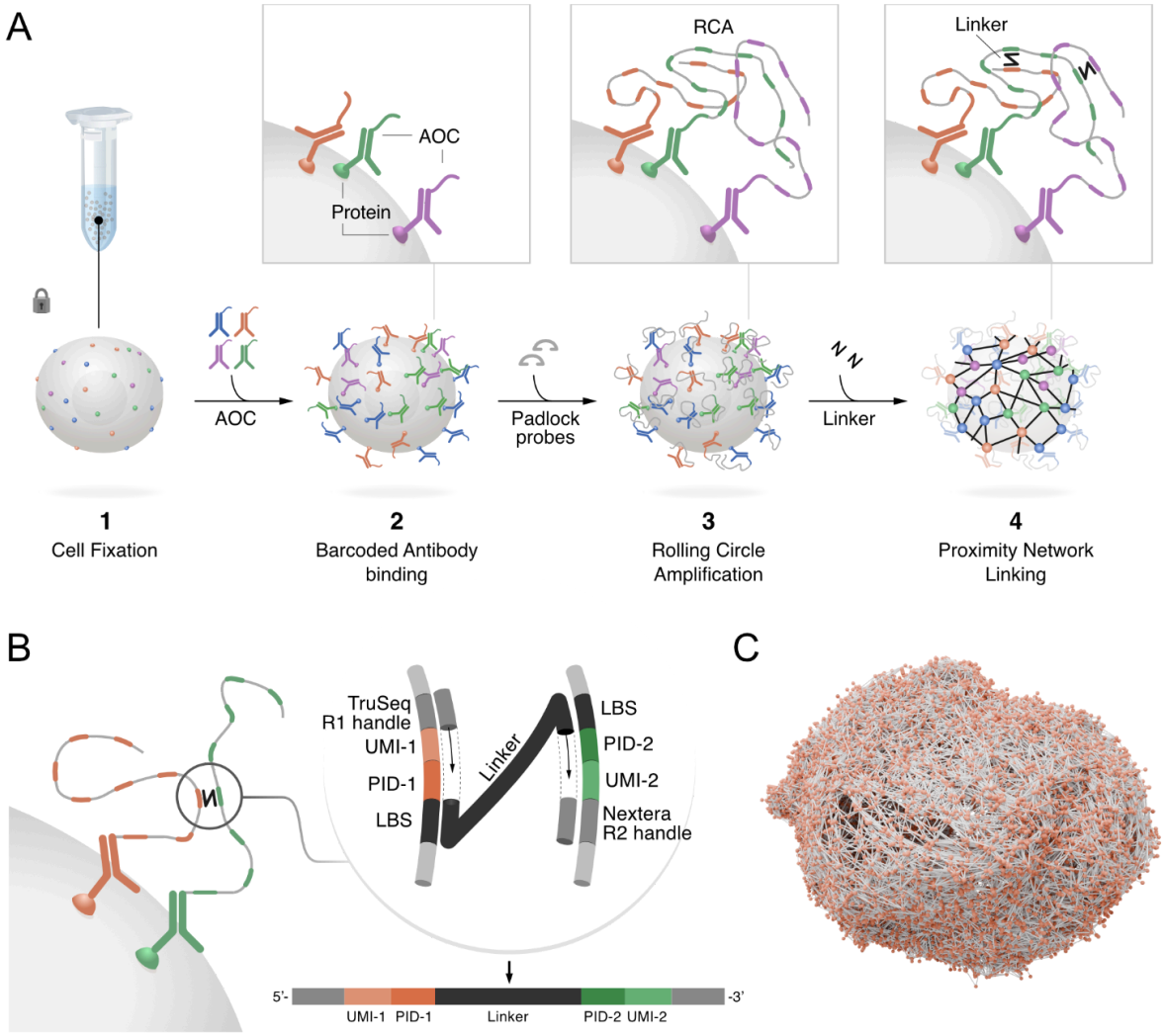

Figure 1. **The Proximity Network Assay connects surface proteins into a cell-wide network.** (A) Proximity Network process steps. 1. Cells are fixed using PFA, 2. Ab-BCs are bound to PFA fixed cells in suspension. 3. Padlock probes are hybridized, followed by gap-fill ligation copying the UMI and Protein ID (PID) of the Ab-BC into the circularized padlock. RCA then makes multiple copies of the UMI and PID. 4. Linker oligonucleotides are hybridized to pairs of proximal RCA products. (B) Overview of linker amplicon construct: Gap-fill ligation incorporates UMI and PID into the target amplicon from two RCA products of type 1 (orange) or type 2 (green), respectively. The amplicon is subsequently PCR:ed and sequenced. (C) 3D reconstruction of the Proximity Network of a single cell. Each node (orange) corresponds to a protein, and each connection a linker molecule.

Proximity Scores as protein interactome networks

To demonstrate spatial analysis by PNA, we assayed 1,017 cells of the Burkitt's lymphoma cell line Raji, a cell line of B cell origin. The Proximity Score used for spatial characterization is formulated as a $\log_2$ ratio comparing observed join counts with the expectation from randomness given the observed count levels of the two markers. As such, a value of 1 can be interpreted as the two markers appearing in proximity of each other twice as often as expected, a value of 2 corresponds to 4 times the expectation, and so on. Similarly, -1 corresponds to half of the expectation, and -2; a quarter. As such, a high value is indicative of colocalization, while a negative value is indicative of spatial segregation between the markers.

The Proximity Scores of Raji cells revealed an intricate landscape of colocalizing and segregating proteins, attesting the existence of multiple protein complexes and microdomains at the cell surface (**Figure 2A**). These include well-known interacting protein pairs such as MHC I (HLA-ABC/B2M), LFA-1 (CD11a/CD18), the B cell receptor (BCR) (CD79a/IgM), and VLA-4 (CD49D/CD29). We could also identify colocalization patterns distinctive of known microdomains including CD20 colocalizing in tetraspanin-rich microdomains (CD37/CD53/CD81/CD82) [23], and GPI-coupled receptors (CD48/CD52/CD55/CD58/CD59) associated with lipid rafts [24]. As expected, high Proximity Scores were found for protein isoforms detected by two probes targeting the same protein but at different epitopes, such as HLA-DR with HLA-DR-DP-DQ, and CD45 with CD45RA and CD45RB.

We then focused on two key proteins of B cell function, and generated a protein interaction network centered on CD19 and CD20 (**Figure 2B**). These two networks were connected since CD19 and CD20 both showed high colocalization with tetraspanins CD37 and CD81. We could detect the recently described interaction between CD20 and CD70 [21], as well as the B cell co-receptor complex formed by CD19 associating with CD81 and CD21, which plays an important role in regulating and enhancing signalling through the BCR [22]. Interestingly, besides this interaction network, CD21 was also associated with a distinct multiprotein domain rich in adhesion molecules including CD49d, CD54 (ICAM-1) and CD102 (ICAM-2).

In addition, Proximity Score results were elevated for many proteins with themselves, which is in concordance with literature reports [25]. Proximity Scores generated by PNA of self-clustering proteins show concordance with immunofluorescence (IF) microscopy images, here exemplified by three proteins with low to high level of clustering (**Figure 2C-E**). CD40 displayed an even distribution across the cell surface, while CD54 and CD81 showed increasingly higher Proximity Score as well as clustering in IF (**Figure 2C-E**).

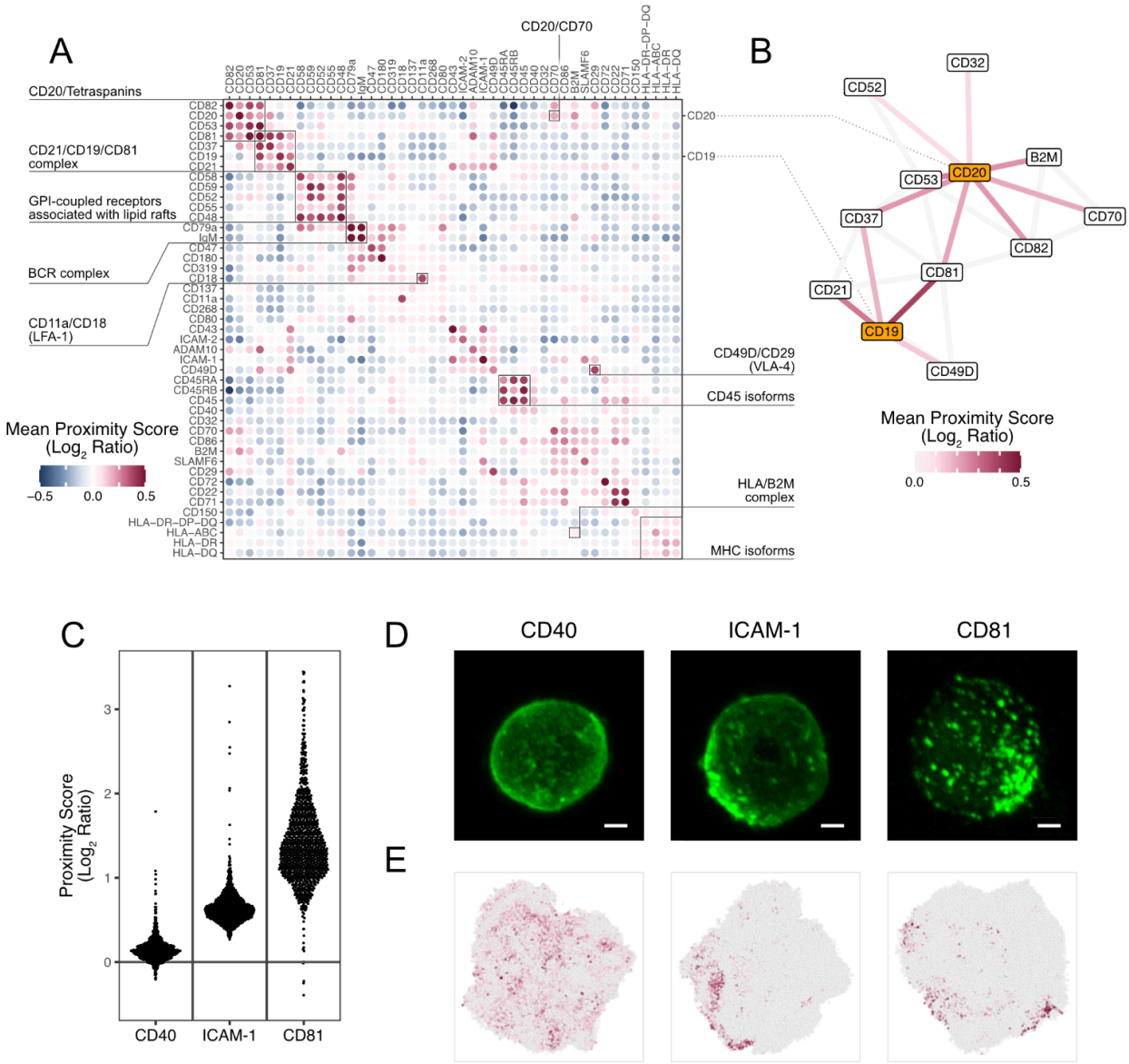

Figure 2. Spatial characterization of the Raji cell surface proxiome. (A) Heatmap of mean Proximity Scores (log2 ratio) of Raji cells showing protein colocalization and self-clustering. Black frames highlight examples of known protein-protein interactions and previously described multi-protein domains. (B) The interaction network of CD19 and CD20, composed of proteins showing mean Proximity Scores above 0.1 with CD19 or CD20. Gray lines indicate mean Proximity Scores above 0.1 between other members of this interaction network. (C) Proximity Scores across Raji cells for the markers CD40, ICAM-1, and CD81. Each point corresponds to the score of a single cell. (D) Representative immunofluorescence (IF) microscopy images of single cells, showing the clustering behavior of CD40, ICAM-1 and CD81. Scale bars: 2 µm. (E) Representative 3D visualizations of PNA cell graphs of single cells showing the distribution of CD40, ICAM-1, and CD81. A darker dot color indicates a high local density of the protein.

Deep phenotyping of heterogenous immune cell populations

The 155-plex panel of the Proxiome kit was developed to cover the most important surface markers to characterize the function and identity of key human immune cell types. To demonstrate the breadth of the panel and the specificity of the included antibodies, we performed a deep annotation of cell types in PBMCs (**Figure 3A-B**). Utilizing a hierarchical annotation strategy (**Supplementary Figure 2**) where cells were divided into gates of increasing granularity to a total of 34 cell type identities, out of which we were able to identify cells of 30 identities, including subtypes of all major PBMC lineages; T cells, B cells, natural killer cells (NKs), dendritic cells (DCs), monocytes, but also small populations of common PBMC contaminant cell types; platelets ($CD41^+$, $CD45^-$) and basophil granulocytes ($CD66b^+$, $CD193^+$). **Figure 3A** shows a UMAP where cell types identified by gating form separate clusters according to expected patterns, exemplified by that various memory compartments of CD4 and CD8 T cells, respectively, clustering together, but distinct from their respective naive CD4/CD8 T cell population.

Identified cell types show expected abundance patterns (**Figure 3C** and **Supplementary Figure 3**), with lineage markers such as CD14 and CD20 distinguishing monocytes and B cells, respectively, and examples of population exclusive expression of T cell receptor (TCR) variants TCRgd, TCRVd2, and TCRVg9 in the gamma delta T cell (gdT) population, which is also the only T cell population that does not express TCRab. To validate the cell annotation, we performed flow cytometry in addition to PNA to quantify a selection of cell populations using an orthogonal method across resting PBMC samples from three different donors. The result showed high concordance between PNA, exemplified by T cells ($CD45^+$, $CD3^+$, PNA: 58.2% vs Flow: 59.4%) (**Supplementary Figure 4A**), as well as the $CD4^+$ (PNA: 57.8% vs Flow: 61.1%) and $CD8^+$ (PNA: 32.8% vs Flow: 28.2%) subsets of T cells (**Supplementary Figure 4B**). The overall correlation of estimated population sizes was very high, with a Pearson's $r = 0.99$ between cell population sizes identified by PNA and Flow cytometry (**Supplementary Figure 4C**). These results confirm the robustness and accuracy of PNA-based cell type annotation in our dataset.

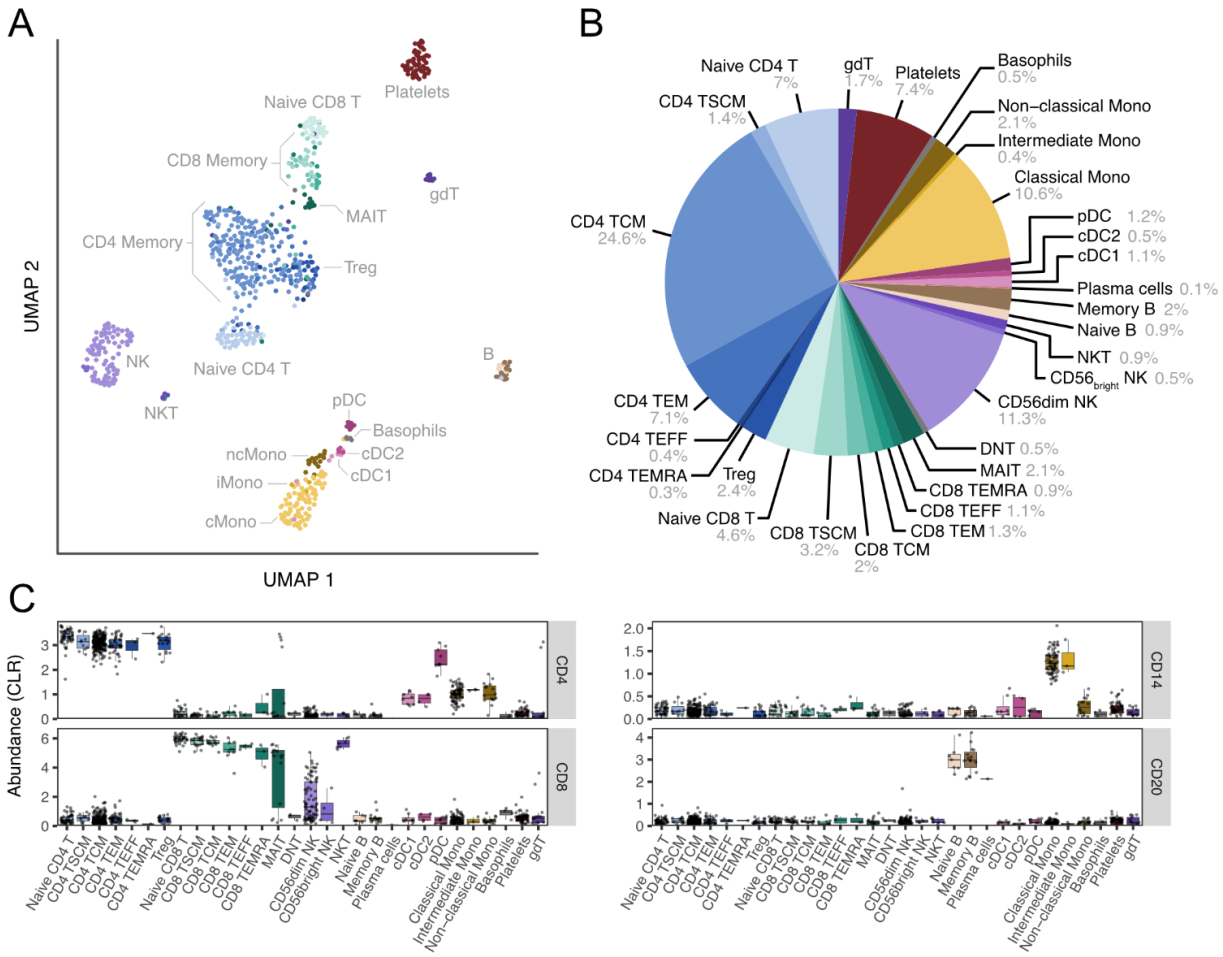

Figure 3. High-dimensional cell type annotation of PBMC samples. (A) UMAP of cell annotation in PBMC. (B) Proportions of found cell types based on abundance of canonical lineage markers. (C) Boxplot of the abundance of markers CD4, CD8, CD14, and CD20 in the various cell types identified.

<u>CAR-T cell Proximity Networks</u>

To evaluate the capacity of PNA for resolving dynamic remodeling of engineered immune cells, we profiled CD19-targeting CAR-T cells before and after coculture with CD19^{+} Raji tumor cells, (**Figure 4**). CAR-T cells were analyzed either in isolation or following coculture at an effector-to-target (E:T) ratio of 1:1 for 4 or 24 hours (**Figure 4A**). Each sample was processed using the 155-plex PNA panel supplemented with a CAR-specific anti-FMC63 probe. Dimensionality reduction based on CLR-transformed protein abundance revealed clear separation of CD4^{+}, CD8^{+}, and Raji cells across all conditions, with approximately 40% of T cells expressing the CD19 CAR (**Figure 4B**).

To characterize CAR-associated interaction landscapes, we computed Proximity Scores between the CD19 CAR and all other targets, generating a network of positively colocalized proteins (**Figure 4C** and **Supplementary Figure 5A**). The CAR receptor exhibited spatial proximity with canonical T cell signaling and adhesion proteins, including TCRαβ, CD5 and

CD6, and multiple ICAM family members. In contrast, the CAR segregated from lipid raft-associated markers such as CD52, CD55 and tetraspanins CD53, and CD81. These results indicate that the synthetic CD19 CAR receptor is not randomly distributed but integrates into endogenous TCR-associated signaling domains while avoiding raft-like compartments, partly mirroring native TCR topology.

Progressive remodeling of the T cell surface proteome was observed during coculture. UMAP clustering of samples based on marker abundance showed clear shifts between monoculture, 4-hour, and 24-hour conditions, with pronounced upregulation of immune activation markers, and downregulation of key activating receptors including the CAR, the TCR and CD28 (**Supplementary Figure 5B)**. Notably, ICAM-1 (CD54) expression increased substantially following coculture (**Figure 4D**). However, 3D spatial rendering revealed that ICAM-1 enrichment occurred in discrete patches rather than uniformly across the cell surface (**Figure 4E**).

Further analysis of these patches showed that they often colocalized with other B cell–specific markers such as CD40, while anti-colocalizing with T cell markers such as CD8 (**Figure 4E**). These findings are consistent with trogocytosis—the transfer of membrane fragments from target to effector cells during immune synapse formation (**Figure 4F**). Visualizations of individual cells showed a range from zero to three or more such tumor-derived patches (**Figure 4G** and **Supplementary Figure 5C)**.

To explore the relationship between patch acquisition and T cell state, we stratified $CD8^+$ cells by canonical activation and exhaustion markers. Cells classified as non-activated ($CD25^-$ $PD\text{-}1^-$) exhibited few or no patches, while activated cells ($CD25^+$ $PD\text{-}1^-$) carried an intermediate patch burden. Exhausted cells ($CD25^+$ $PD\text{-}1^+$) displayed the highest frequency and number of tumor patches, with a ~5-fold increase in patch count relative to baseline (**Figure 4G)**. These results suggest that PNA enables functional stratification of immune effector cells based on spatial acquisition of tumor-derived proteins, a key advantage over expression-only assays.

In addition to detecting trogocytosis, PNA enabled identification of direct T cell-tumor cell conjugates. Proximity Networks of conjugated cell pairs revealed clear localization of T cell-specific markers (e.g. CD3e) on one side and B cell markers (e.g. CD40) on the opposite pole (**Figure 4H**). This pattern was distinct from trogocytic patching and consistent with immune synapse formation. Such conjugates can be distinguished by PNA from trogocytic cells, providing a high-resolution approach for identifying physical immune engagements and mapping the molecular topology of intercellular contact interfaces.

Together, these results demonstrate that PNA captures the nanoscale organization and dynamic remodeling of the CAR-T cell surface during tumor interaction, including co-receptor colocalization, ligand acquisition via trogocytosis, and synapse formation.

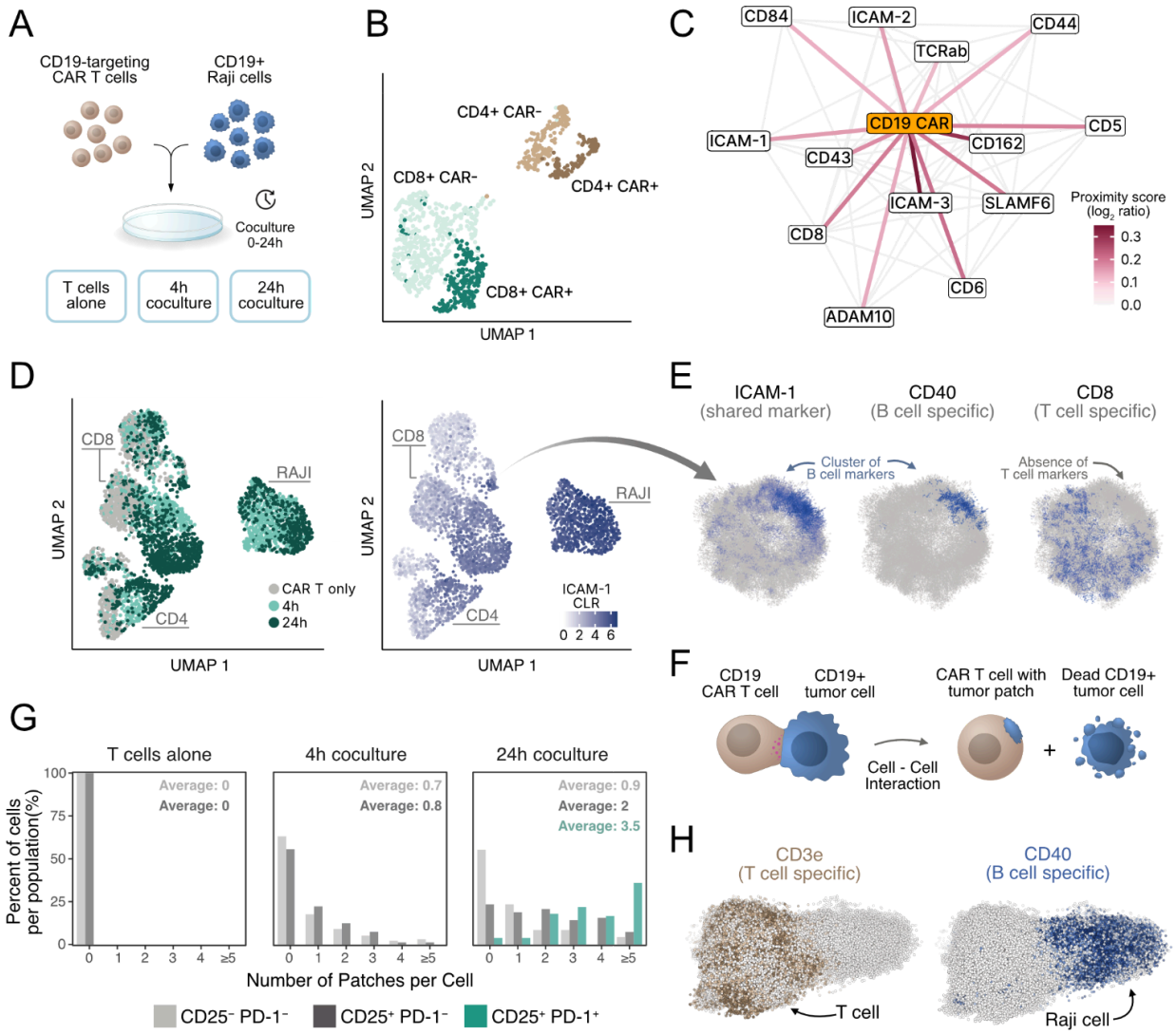

Figure 4. **The Proximity Network Assay resolves CAR-T cell surface remodeling, trogocytosis, and tumor cell conjugation**. (A) Workflow for functional characterization of CAR-T cells. CAR-T cells were either kept separate, or were mixed with CD19-positive Raji cells at an 1:1 E:T ratio. Cells were cocultured for either 4h or 24h, after which they were retrieved and fixed using 1 % PFA. Each sample was split into two duplicates and processed with the Proximity Network Assay according to the DP001 CAR Barcoded Antibody spike-in Proxiome kit (v1.00) manual. (B) The CAR-T cell population included both $CD4^+$ and $CD8^+$ subsets, with ~40% of cells expressing the CD19 CAR transgene. (C) Proteins displaying positive colocalization (average score ≥0.1) with the CD19 CAR were plotted in a network (the CD19 CAR Proxiome). Positive colocalization scores for protein pairs other than the CD19 CAR have been grayed out for clarity. (D) Left: High-dimensional clustering based on protein abundance data for CAR-T cells alone, 4h cocultured cells, and 24h cocultured cells efficiently separating CD4, CD8 and Raji cells. Right: Cocultured T cells displayed increased levels of ICAM-1. (E) 3D visualization of a single CD8 T cell from the 24h cocultured sample. The cell displays a patchy ICAM-1 distribution where the patch colocalized with B cell markers like CD40, while anti-colocalizing with T cell marker CD8. (F) Illustration showcasing the process of trogocytosis, exchange of plasma membrane between cells, in CAR-T cells.

(G) Quantification of tumor patches on the surface of $CD8^+$ non-activated ($CD25^-$, $PD\text{-}1^-$), activated ($CD25^+$, $PD\text{-}1^-$) and exhausted ($CD25^+$, $PD\text{-}1^+$) T cells. (H) An example of a CD8 T: Raji cell conjugate. The T cell (left) displays expression of T cell specific marker CD3e, while the Raji cell (right) expresses B cell marker CD40.

Systemic lupus erythematosus (SLE) study

To investigate whether single cell protein interactomics data by PNA can serve as a novel type of biomarker or provide new insights into disease mechanisms of auto immune disorders we profiled B cells from patients with systemic lupus erythematosus (SLE, n = 2) and healthy controls (Controls, n = 2). Among our findings, CD21 was down-regulated in SLE-patients (Wilcoxon $p = 3.6 \times 10^{-12}$) (**Figure 5A)**. CD21 is a complement receptor and key component of the B cell co-receptor complex, where it enhances signalling through the B cell receptor (BCR) [26]. Reduced CD21 expression on B-cells in SLE-patients has previously been reported and associated with high disease activity [27]. Interestingly, we also observed that CD21 exhibit higher Proximity Score in SLE compared to controls (Wilcoxon $p = 1.2 \times 10^{-10}$), indicating that CD21 protein molecules cluster within a confined part of the cell membrane i.e. exhibiting a polarized CD21-receptor concentrate in lupus B cells (**Figure 5A-B**). Such a clustered spatial organization has previously not been reported, but could serve to focus and amplify local signalling from complement-decorated immune complexes in B-cells, or could be a secondary consequence of increased immune complexes in circulation forcing the CD21 molecules in proximity. Alternatively, it might be a compensatory mechanism by the B-cells to remove CD21 away from active signalling hubs to dampen chronic B cell activation, but further investigation will be required to understand the consequences of such polarized CD21 expression. The PNA platform offers a promising approach to longitudinally monitor and profile CD21 topology in SLE patients, track changes during disease flares, and assess whether biological therapies can restore a more physiological, symmetric distribution of CD21.

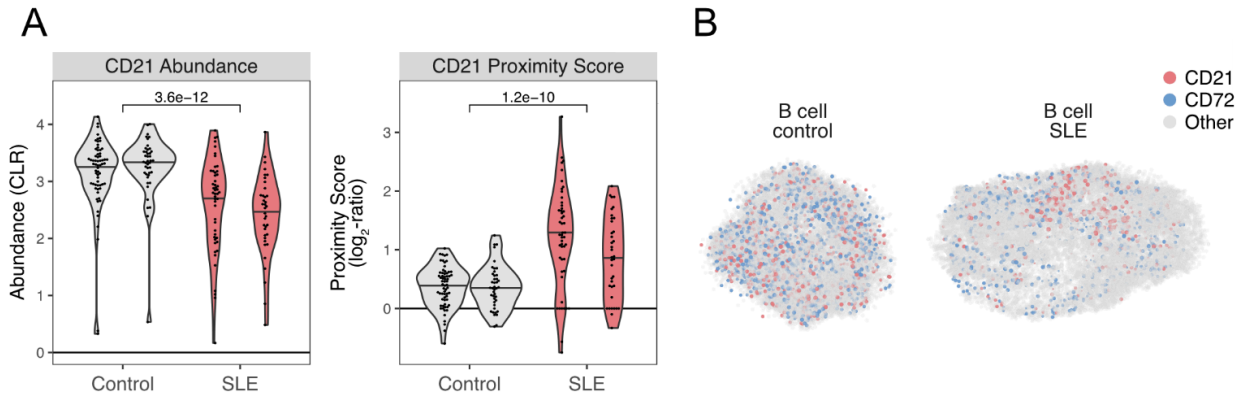

Figure 5. SLE B cells display increased clustering of CD21. Protein abundance and spatial organization was assessed for SLE compared to healthy B-cells from two PBMC samples of each type. (A) Violin plots of abundance (left) and Proximity Score (right) of CD21. (B) 3D plots of two representative cells; healthy control B-cell (left) and a SLE B-cell (right) illustrating increased clustering of CD21.

Discussion

The functional state of a cell is defined not only by its transcriptomic or proteomic composition, but critically by the spatial organisation of its proteins through clustering, segregation, and interactions. This protein interactome governs essential cellular processes such as signal transduction, immune activation, and cell-cell communication. Yet, despite its biological significance, spatial protein organisation remains poorly resolved at the single-cell, omics-scale level.

Existing tools for protein interaction studies either lack throughput or resolution, or require bulk input from homogeneous cell populations. For instance, proximity labeling (PL) techniques such as BioID and APEX, read out by mass spectrometry, have enabled discovery of thousands of interaction partners in a bulk format, but require tens of millions of cells and achieve limited spatial resolution (~200-300 nm) [28,29], These approaches are unsuitable for studying heterogeneous clinical samples, where cell-type-specific spatial phenotypes are critical for biomarker discovery and translational research.

The Proximity Network Assay addresses this unmet need by enabling high-throughput, single-cell, nanoscale interactomics through a DNA-sequencing-based readout. The presented implementation of PNA for cell surface analysis captures the proximity profile of 155 antibody-targeted proteins, with demonstrated applications in human immune cells, cell lines, and CAR-T cells. This is achieved without the need for single cell compartmentalization as the method generates an interconnected spatial network of barcodes for each assayed cell.

PNA extends the conceptual framework of DNA-based proximity methods such as PLA and PEA [16,17], which rely on pairwise proximity detection via sequence generation. Unlike these pairwise assays, PNA constructs comprehensive networks of protein proximities, enabling analysis of abundance, spatial self-clustering of one protein species, and colocalization of protein pairs. This generalisation from binary interactions to spatial network topology distinguishes PNA from prior proximity technologies. It also represents an advancement over our earlier Molecular Pixelation (MPX) platform [9], which demonstrated optics-free spatial reconstruction but with lower spatial resolution compared to PNA which provides a unique spatial position for each detected protein.

PNA is validated by its ability to detect well-characterised molecular complexes, such as HLA-ABC/β2-microglobulin, CD19/CD81, IgM/CD79a, integrin complexes, and more. Spatial proximity metrics may serve as interaction-based biomarkers, including for response prediction to immune checkpoint inhibitors [30], or for investigating CAR-T cell phenotypes [31]. However, as with all proximity-based approaches, a high Proximity Score does not confirm direct physical interaction. It may reflect nanoclustering, shared membrane microdomains, or subcellular colocalization [25]. This distinction is important when interpreting interaction candidates.

Nevertheless, the reproducible detection of known complexes and consistent clustering patterns supports the utility of PNA in hypothesis generation, mechanistic inference, clinical biomarker discovery, and support development of therapy-induced spatial remodelling of surface proteins [32]. The identification of novel protein interactions that are prevalent on cancer cells and aberrant immune cells in comparison to healthy cells is of particular interest, as these may constitute novel drug targets using bispecific antibodies and CAR-T cells potentially increasing the number of druggable cell surface targets.

The graph-native structure of PNA data opens new analytical possibilities suited for machine learning, including graph convolutional networks (GCNs) and graph attention models [33]. These algorithms can identify latent structure, classify spatial phenotypes, and predict cell state transitions or therapeutic outcomes from network topology.

Looking forward, the multi-modal potential of PNA is considerable. Preliminary findings show that Proximity Networks can be generated within cells, enabling nanoscale localization of intracellular proteins in signaling pathways and immune synapse protein interactions between cells (work in progress). We also anticipate expansion into transcriptomics using RNA probes.

The Proximity Network Assay has the potential to impact single cell protein interactomics beyond what's achievable through traditional microscopy which is limited in resolution, multiplexing, and throughput. PNA requires approximately 300,000 sequencing reads per cell and is compatible with existing NGS platforms. As sequencing technologies continue to advance [34] the output of PNA data will increase further, making analyses of larger sample areas such as tissue become feasible..

Current single cell research is based on parts-list abundance measurements of transcripts and proteins per cell. Single cell protein interactomics enabled by the Proximity Network Assay adds a new nanoscale spatial omics layer, to gain novel insights into the molecular mechanisms of cell function.

Acknowledgements

Author Contributions Statement

FK and SF conceived of the Proximity Network Assay. FK, SF, CG, TK, DT, HvO, LL, MK, JB, CM, MaS, MiS, HvO, PB, RF, EN, developed the method and/or performed experiments. FK, AMB, JD, FdT, PT, LL, MK, developed the data analysis algorithms and the pipeline. FK, MK, VvH, AMB, PB, HvO, DT, SP, LF, RF, PB performed in depth analyses and interpretation of biological results. FK, MK, HvO, VvH, PB, and SF wrote the manuscript. All the authors have read and approved the manuscript before submission.

Competing interests

All authors (except RF and EN) are employees or advisors to Pixelgen Technologies AB commercializing products based on Proximity Networks. They are also shareholders, advisors, or stock option holders of the company. Proximity Networks and Proxiome are trademarks of Pixelgen Technologies AB.

Ethics declaration

All samples acquired from the Karolinska Hospital with informed consent and withheld sample identity or other medical information.

Methods

PBMC extraction from buffy coats

Buffy coats derived from healthy, anonymous donors, were acquired from Komponentlab, Karolinska hospital. The blood was diluted and the PBMCs were isolated through density gradient centrifugation using Lymphoprep (Stemcell technologies). The platelet fraction was reduced by 3 repeated low-speed centrifugation steps, after which remaining red blood cells were lysed using eBioscience RBC lysis buffer (Invitrogen). Resting cells were either fixed using 1% paraformaldehyde (PFA) and frozen, or activated for 72h using Phytohemagglutinin (PHA) in RPMI supplemented with 10% FBS and 1% Penicillin-Streptomycin. Following activation, cells were fixed with 1% PFA and frozen for long-term storage.

Cell culture

Raji cells were cultured in RPMI media supplemented with 10% fetal bovine serum and 1% Penicillin-Streptomycin and were split every 48 hours. Cell cultures were regularly confirmed negative for mycoplasma contamination.

CD19 CAR-T cell - tumor cell coculture

CD19-targeting CAR-T cells (Promab) were thawed and washed, after which they were fixed using 1% PFA, or cocultured with Raji cells at an E:T ratio of 1:1 for 4 or 24 hours in U-bottom 96-well plates. After the indicated time, cocultured cells were harvested and fixed using 1% PFA, and frozen and stored before running PNA.

Microscopy of PNA products

Millicell® EZ Slides were coated with 0.1% (w/v) poly-L-lysine for 5 minutes, then air-dried at room temperature. PBMCs were fixed and blocked according to the PNA protocol. The RCA reaction was spiked with 1ul of 1mM Fluorescin-dUTP. After RCA, cells were washed twice, and subsequently stained with AF647-conjugated Wheat Germ Agglutinin (WGA). The suspension was added to a coated EZ Slide well and incubated overnight at 4 °C to allow cells to settle. The next day, slides were mounted with SlowFade™ Glass Soft-set Antifade Mountant containing Dapi. Slides were imaged in 3D on a Zeiss LSM 980 using the Airyscanning module and a 63X (1.4) oil objective. Analysis was performed using ImageJ. Images were corrected for spectral

drift and brightness and contrast adjusted. 3D stack were compiled, and intensity profiles were measured for single optical planes for the WGA and PNA-product channels.

Comparison of PNA and flow cytometry for cell type identification

PBMC cells from 3 different donors were fixed using 1% PFA, washed and analyzed using PNA, or stained for flow cytometry using CD45 Pe, CD3 PeCy7 and CD56 APC, or CD45 Pe and CD8 AF488, or CD45 Pe and CD4 Fitc, or CD45 Pe and CD19 AF700, or CD45 Pe and CD14 APC, or CD4 Pe, CD3 PeCy7 and CD8 AF488. Cells were processed on a CytoFLEX (Beckman Coulter) and analyzed using FlowJo. Cells were gated for: ($CD14^+$, $CD45^+$), ($CD19^+$, $CD45^+$), ($CD3^+$, $CD45^+$), ($CD56^+$, $CD45^+$), ($CD8^+$, $CD3^+$), ($CD4^+$, $CD3^+$), ($CD3^+$, $CD4^+$, $CD8^-$), ($CD3^+$, $CD8^+$, $CD4^-$).

Microscopy of protein clustering in Raji cells

Raji cells were fixed using 1% PFA, washed and analyzed using PNA, or stained for microscopy using either mouse anti-human CD40, mouse anti-human CD81 or mouse anti-human ICAM-1, followed by secondary staining using an anti-mouse AF647-conjugated monovalent nanobody (Chromotek). Cells were spotted and mounted on glass slides using SlowFade gold (Invitrogen). Slides were imaged in 3D on a Zeiss LSM 980 using the Airyscanning module and a 63X (1.4) oil objective. Using ImageJ, images were adjusted for brightness and contrast and max intensity projections were produced.

Proximity Network Assay

Manufacturer's instructions were followed for the Pixelgen Proxiome Kit. In short, samples were first fixed in 1% PFA, blocked, then stained overnight at +4C using a pool of 155 barcoded target specific antibodies and 3 mouse isotype controls, containing either type 1 or type 2 oligonucleotide sequence. Cells were then washed and antibody barcodes subjected to localized rolling circle amplification of gap-filled padlock probes for 10 minutes followed by addition of linker oligonucleotides designed to hybridize to two proximal RCA products of type 1 and 2. Gap-fill ligation was then performed to incorporate the UMI and PID sequences of the RCA products onto the hybridized linker oligonucleotide. One thousand cells were then transferred to a PCR amplification reaction to amplify the generated amplicons, followed by a second PCR reaction to attach sequencing adapters..

The PCR products were purified using SPRIselect beads, and quantified using Qubit hsDNA assay according to instructions of the Pixelgen Proxiome kit. The purified and quantified products were diluted to either 0.65 nM for Illumina P2 Xleap kits, or 0.49 nM for Illumina P3 and P4 Xleap kits and spiked with 15% PhiX and paired-end sequenced on an Illumina NextSeq2000 sequencing system, using 44 cycles for Read 1 and 78 cycles for Read 2.

Data processing

PNA sequencing data were processed using Pixelator; an in-house open-source data analysis pipeline implemented in nextflow nf-core/pixelator (https://github.com/nf-core/pixelator). Downstream analyses were performed in R using pixelatorR v0.13.0

(https://github.com/PixelgenTechnologies/pixelatorR) and Seurat v5.2.1. For graphical visualizations, ggplot2 v3.5.1 and ComplexHeatmaps v2.22.0 were used.

Join Count statistics

The Proximity Score was used to assess the degree of association between two markers in a component graph, and is based on join count statistics [20]. The developed algorithm tracks the number of edges between marker pairs in a component, called "join count", corresponding to the number of times instances of the two marker species were adjacent to each other. In order to understand whether the join count was higher or lower compared to chance, a baseline expectation was calculated using Monte Carlo simulations, where the spatial distribution of markers was randomized while the graph structure and marker abundance were kept constant. For each graph component (corresponding to a single cell) 100 such permutations were created, forming a null distribution that describes the join count of pairs of markers if they were randomly placed as node attributes on the graph, enabling comparison of the observed patterns to random expectation.

Using the mean (*E*) and standard deviation (*σ*) of the simulated null distribution, the join counts (*x*) were formulated as a log2 ratio (L):

$$L = log_2(\frac{x}{E}) \quad (1)$$

And a Z-score (Z):

$$Z = \frac{x - E}{\sigma} \quad (2)$$

Patch detection

Patches were detected by expanding the adjacency matrix of a component to include the k-th neighbours (k = 2) followed by subsetting this expanded adjacency matrix to nodes that are labeled by B-cell originating patch-specific markers CD20, CD22 and CD40 as well as the nodes connecting these patch-specific marker nodes. A new graph was created from the subsetted adjacency matrix and the graph was split into its connected components representing the different patches. Next, Leiden iterative community detection was used to split up weakly connected patch components (resolution parameter = 0.01) and patches smaller than 200 nodes were filtered out.

References

1) Al-Aghbar MA, Jainarayanan AK, Dustin ML, and Roffler SR. The interplay between membrane topology and mechanical forces in regulating T cell receptor activity. *Commun Biol* Jan 11;5(1):40 (2022)
2) Dustin M.L. The immunological synapse *Cancer Immunol Res.* Nov; 2(11): 1023–1033. (2014)
3) Vigano S, Utzschneider DT, Perreau M, Pantaleo G, Zehn D., and Harari A. Functional Avidity: A Measure to Predict the Efficacy of Effector T Cells? *Clinical and Developmental Immunology.* Volume 2012, Article ID 153863 (2012)
4) Mañes S, Gómez-Moutón C, Lacalle RA, Jiménez-Baranda S, Mira E., Martínez-A C, Mastering time and space: immune cell polarization and chemotaxis. *Review Semin Immunol.* Feb;17(1):77-86. (2005)
5) Lu H, Zhou Q, Jun He, Jiang Z, Peng C, Tong R & Shi J. Recent advances in the development of protein–protein interactions modulators: mechanisms and clinical trials. *Signal Transduction and Targeted Therapy* volume 5, Article number: 213 (2020)
6) Rudnicka D., Oszmiana A, Finch DK, Strickland I, Schofield DJ, Lowe DC, Sleeman MA, Davis DM Rituximab causes a polarization of B cells that augments its therapeutic function in NK-cell–mediated antibody-dependent cellular cytotoxicity. *Blood* 121 (23): 4694–4702. (2013)
7) Söderberg O, Gullberg M, Jarvius M, Ridderstråle K, Leuchowius KJ, Jarvius J, Wester K, Hydbring P, Bahram F, Larsson LG, Landegren U. Direct observation of individual endogenous protein complexes in situ by proximity ligation. *Nat Methods*. Dec;3(12):995-1000. (2006)
8) Chandrasekharan G, Unnikrishnan M. High throughput methods to study protein-protein interactions during host-pathogen interactions. *European Journal of Cell Biology.* Volume 103, Issue 2, June 2024, 151393
9) Karlsson F, Kallas T, Thiagarajan D, Karlsson M, Schweitzer M, Fernandez Navarro J, Leijonancker L, Geny S, Pettersson E, Rhomberg-Kauert J, Larsson L, van Ooijen H, Petkov S, González-Granillo M, Bunz J, Dahlberg J, Simonetti M, Sathe P, Brodin P, Martinez Barrio, A, Fredriksson S, Molecular pixelation: spatial proteomics of single cells by sequencing. Nature Methods volume 21, pages1044–1052 (2024)
10) Boulgakov AA, Ellington AD, Marcotte EM. Bringing Microscopy-By-Sequencing into View. *Trends Biotechnol.* Feb;38(2):154-162. (2020)
11) Hoffecker IT, Yang Y, Bernardinelli G, Orponen P, Högberg B. A computational framework for DNA sequencing microscopy. *Proc Natl Acad Sci U S A.* Sep 24;116(39):19282-19287. (2019)
12) Weinstein JA, Regev A, Zhang F. DNA Microscopy: Optics-free Spatio-genetic Imaging by a Stand-Alone Chemical Reaction. *Cell*. Jun 27;178(1):229-241.e16. (2019)
13) Abdulraouf A., Jiang W., Xu Z., Zhang Z., Isakov S., Raihan T., Zhou W., and Cao J. Optics-free Spatial Genomics for Mapping Mouse Brain Aging bioRxiv 2024.08.06.606712; doi: https://doi.org/10.1101/2024.08.06.606712
14) Liao H., Kottapalli S., Huang Y., Chaw M., Gehring J., Waltner O., Phung-Rojas M., M. Daza R., A. Matsen IV F., Trapnell C., Shendure J., and Srivatsan S. Optics-free reconstruction of 2D images via DNA barcode proximity graphs. bioRxiv 2024.08.06.606834; doi: https://doi.org/10.1101/2024.08.06.606834
15) Qian, N., Weinstein, J.A. Spatial transcriptomic imaging of an intact organism using volumetric DNA microscopy. Nat Biotechnol (2025). https://doi.org/10.1038/s41587-025-02613-z
16) Fredriksson S, Dixon W, Ji H, Koong AC, Mindrinos M, Davis RW. Multiplexed protein detection by proximity ligation for cancer biomarker validation. *Nat Methods*. Apr;4(4):327-9. (2007)
17) Lundberg M, Eriksson A, Tran B, Assarsson E, Fredriksson S. Homogeneous antibody-based proximity extension assays provide sensitive and specific detection of low-abundant proteins in human blood. *Nucleic Acids Res*. Aug;39(15):e102. (2011)

18) Feng W, Beer JC, Hao Q, Ariyapala IS, et al.NULISA: a proteomic liquid biopsy platform with attomolar sensitivity and high multiplexing. Nature Communications volume 14, Article number: 7238 (2023)
19) Majstoravich S. et al Lymphocyte microvilli are dynamic, actin-dependent structures that do not require Wiskott-Aldrich syndrome protein (WASp) for their morphology Blood. Sep 1;104(5):1396-403. 2004
20) Moran PAP, The Interpretation of Statistical Maps. Journal of the Royal Statistical Society: Series B (Methodological), Volume 10, Issue 2, July 1948, Pages 243–251
21) Arp AB, et al. CD70 recruitment to the immunological synapse is dependent on CD20 in B cells. PNAS April 15, 2025122 (16) e2414002122
22) Wentink MWJ, Zelm MC, van Dongen JJM, Warnatz K, Mirjam van der Burg M. Deficiencies in the CD19 complex Clin Immunol. 2018 Oct:195:82-87.
23) Pavlasova G, Mraz M, The regulation and function of CD20: an “enigma” of B-cell biology and targeted therapy. Hematologica. Vol. 105 No. 6 (2020): June, 2020
24) Loertscher R. Lavery P. The role of glycosyl phosphatidyl inositol (GPI)-anchored cell surface proteins in T-cell activation. Transplant Immunology Volume 9, Issues 2–4, May 2002, Pages 93-96
25) Garcia-Parajo MF, Cambi A, Torreno-Pina JA, Thompson N, Jacobson K. Nanoclustering as a dominant feature of plasma membrane organization. J Cell Sci (2014) 127 (23): 4995–5005.
26) Cherukuri A, Cheng PC, Pierce SK. The role of the CD19/CD21 complex in B cell processing and presentation of complement-tagged antigens. J Immunol. 2001 Jul 1;167(1):163-72.
27) Gjertsson I, McGrath S, Grimstad K, Jonsson CA, Camponeschi A, Thorarinsdottir K, Mårtensson IL, A close-up on the expanding landscape of CD21–/low B cells in humans. Clin Exp Immunol. 2022 Nov 16;210(3):217–229.
28) Carlos AJ, Yang D, Thomas DM, Huang S, Harter KI, Moellering RE. Family-Wide Photoproximity Profiling of Integrin Protein Social Networks in Cancer. bioRxiv 2024.09.18.613588
29) Floyd BM, Schmidt EL, Till NA, Yang JL, Liao P, George BM, Flynn RA, Bertozzi CR. Mapping the nanoscale organization of the human cell surface proteome reveals new functional associations and surface antigen clusters. bioRxiv 2025.02.12.637979
30) Yaghoubi Naei VY, Tubelleza R, Monkman J, Sadeghirad H, Donovan ML, Blick T, Wicher A, Bodbin S, Stad R, Basu S, Cooper C, Barnett C, Ken O'Byrne K, Ladwa R, Warkiani ME, Hughes BGM, Kulasinghe A, Spatial interaction mapping of PD-1/PD-L1 in Head and Neck Cancer reveals the role of Macrophage-Tumour Barriers associated with immunotherapy response Research Square. https://doi.org/10.21203/rs.3.rs-5398442/v2
31) Cesnik A., Roth T., Takasci-Nagy O., Le T., Satpathy A., Lundberg E., Single-cell molecular pixelation of CAR T cell surface proteome reveals spatial patterns characteristic of chronic stimulation. 23rd HUPO meeting 2024
32) Till NA, Ramanathan M, Bertozzi CR, Induced proximity at the cell surface. Nature Biotechnology volume 43, pages702–711 (2025)
33) Cai S, Hu T, Venkataraman A, Rivera Moctezuma FG, Ozturk E, Zhang N, Wang M, Zvidzai T, Das S, Pillai A, Schneider F, Ramalingam SS, Oh Y-T, Sun S-Y & Coskun AF. Spatially resolved subcellular protein–protein interactomics in drug-perturbed lung-cancer cultures and tissues. Nature Biomedical Engineering (2024)
34) Kokoris M *et al*. Sequencing by Expansion (SBX) – a novel, high-throughput single-molecule sequencing technology. bioRxiv 2025.02.19.639056

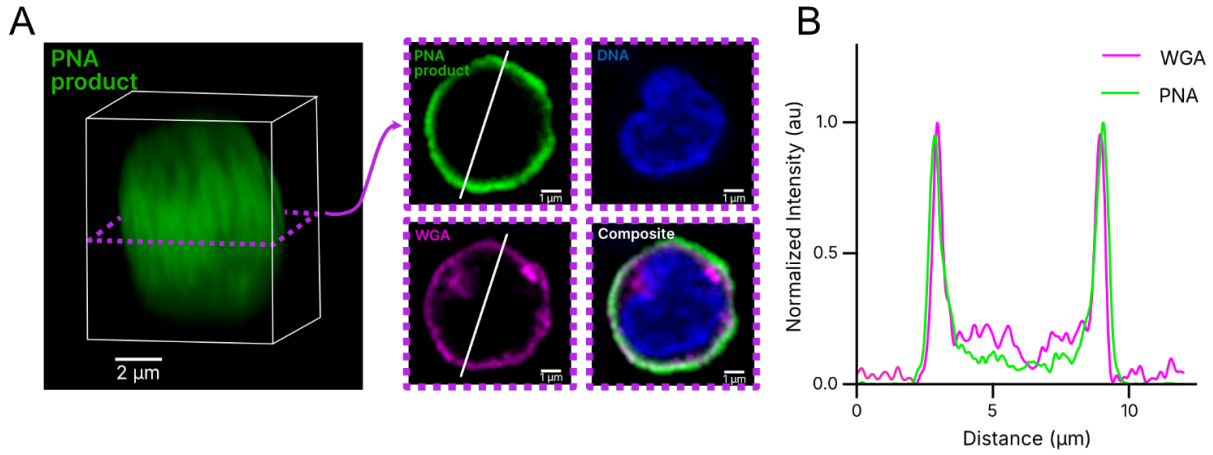

Supplementary Figure 1. Distribution of PNA reaction products at the cell surface. (A) Fluorescence microscopy image of PNA products surrounding a single immune cell. The RCA reaction was supplemented with fluorescently labelled nucleotides to visualize the cell surface coverage with PNA products. Left, 3D reconstruction; Right, single imaging plane. (B) Fluorescence intensity profiles for WGA (labelling the plasma membrane) and PNA products along the line indicated in (A), demonstrating specific localization of the product to the cell membrane.

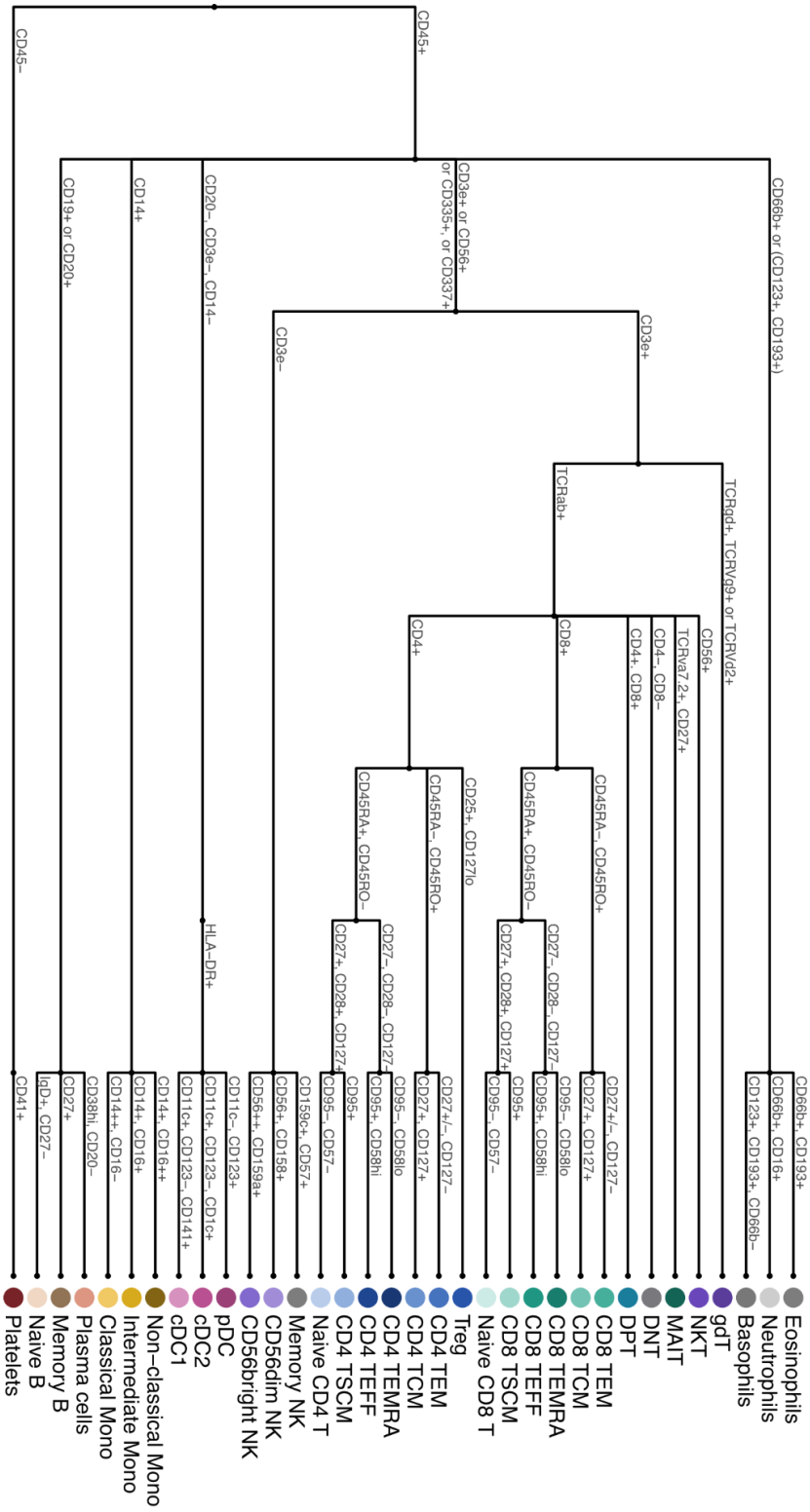

Supplementary Figure 2. Hierarchical annotation strategy of cell types.

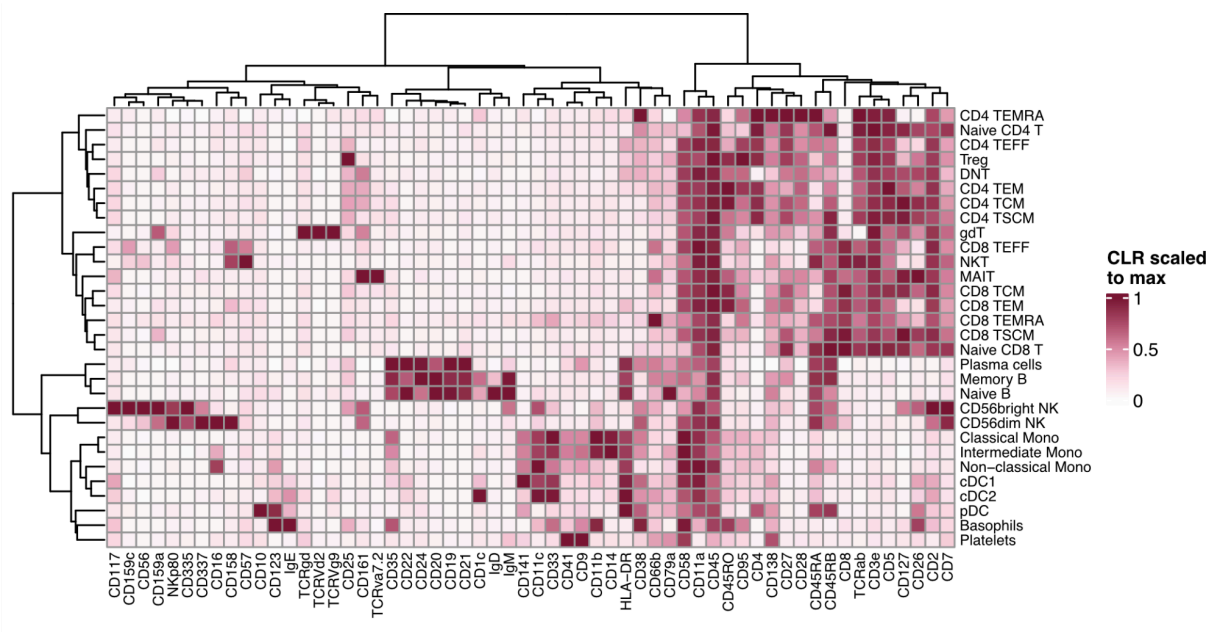

Supplementary Figure 3. Heatmap of relative mean abundance level across annotated cell types in PBMCs. The mean abundance (CLR) has here been max-scaled such that the population with the highest abundance has a value of 1.

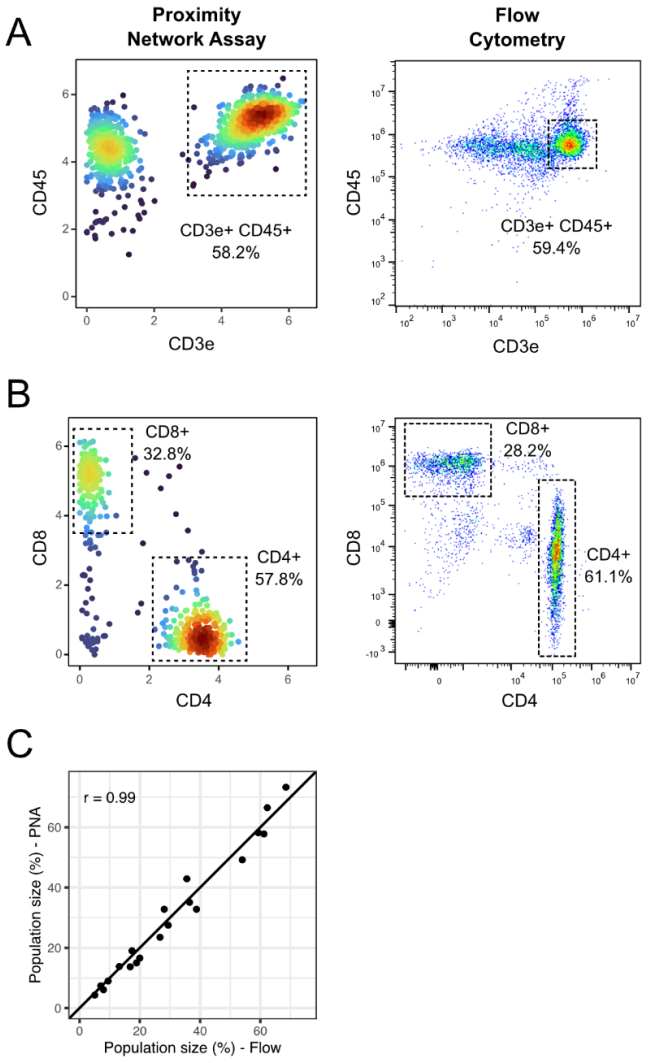

Supplementary Figure 4. Comparison of the Proximity Network Assay and Flow Cytometry for cell identification. (A) Gating of T cells using density plots for CD3e and CD45 for PNA (left) and flow cytometry (right). (B) Gating of CD4 T cells ($CD4^+$, $CD8^-$) and CD8 T cells ($CD8^+$, $CD4^-$) for PNA (left) and flow cytometry (right). (C) Scatter plot showing the correlation between PNA and flow cytometry for the detection of up to 8 unique cell populations in 3 different biological donors (20 identified populations).

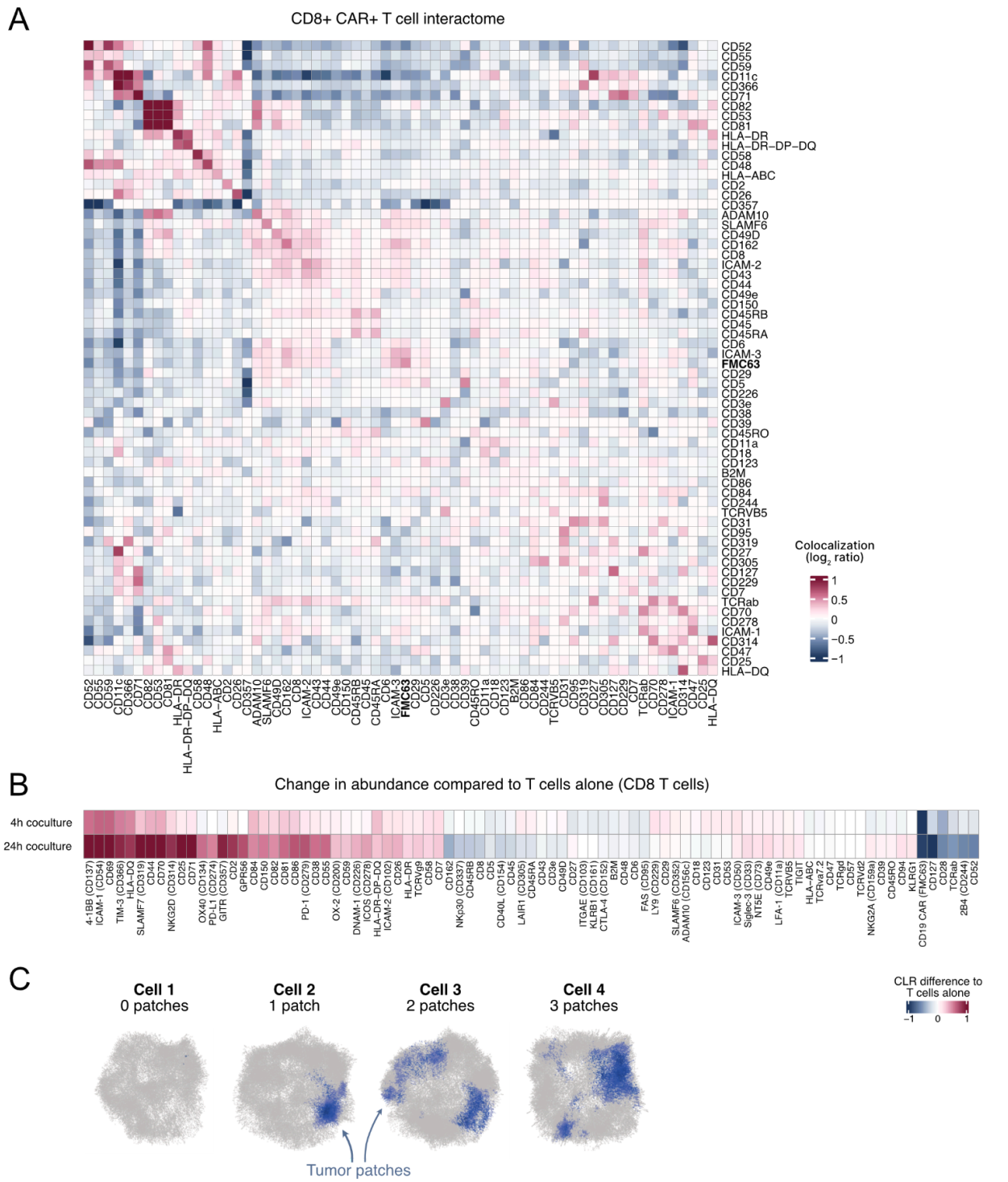

Supplementary Figure 5. Proxiome profile of CD19 CAR-T cells. (A) Heatmap of mean Proximity Scores (log2 ratio) of CD8$^+$ CAR-T cells showing protein colocalization and self-clustering. (B) Average differential protein abundance of 4h- and 24h cocultured CD8 T cells compared to cells cultured alone. Axis has been capped at -1 and 1. (C) Representative 3D visualizations of 4 different PNA cell graphs containing various amounts of Raji-derived membrane patches.